Nanoscale Advances

ROYAL SOCIETY OF CHEMISTRY

PAPER

View Article Online
View Journal | View Issue

Cite this: *Nanoscale Adv.*, 2021, **3**, 2870

Deposition pressure-induced microstructure control and plasmonic property tuning in hybrid ZnO–Ag_xAu_{1-x} thin films†

Robynne L. Paldi,[a] Xing Sun,[a] Xin Li Phuah,[a] Juanjuan Lu,[a] Xinghang Zhang,[a] Aleem Siddiqui[c] and Haiyan Wang *[ab]

Received 22nd October 2020
Accepted 20th February 2021

DOI: 10.1039/d0na00887g

rsc.li/nanoscale-advances

Self-assembled oxide–metallic alloy nanopillars as hybrid plasmonic metamaterials (*e.g.*, ZnO–Ag_xAu_{1-x}) in a thin film form have been grown using a pulsed laser deposition method. The hybrid films were demonstrated to be highly tunable *via* systematic tuning of the oxygen background pressure during deposition. The pressure effects on morphology and optical properties have been investigated and found to be critical to the overall properties of the hybrid films. Specifically, low background pressure results in the vertically aligned nanocomposite (VAN) form while the high-pressure results in more lateral growth of the nanoalloys. Strong surface plasmon resonance was observed in the UV-vis region and a hyperbolic dielectric function was achieved due to the anisotropic morphology. The oxide–nanoalloy hybrid material grown in this work presents a highly effective approach for tuning the binary nanoalloy morphology and properties through systematic parametric changes, important for their potential applications in integrated photonics and plasmonics such as sensors, energy harvesting devices, and beyond.

Introduction

Bimetallic nanoalloys are a class of materials poised to present promising applications in nanotechnology.[1–4] For example, Ag_xAu_{1-x} (ref. 5) and Au_xCu_{1-x} (ref. 6) are capable of being used in optical and plasmonic applications, where the plasmon resonance is easily controlled through manipulation of the composition and morphology. Other promising nanoalloys are magnetic compositions such as Fe_xCo_{1-x} (ref. 7) for magnetic storage memory, where properties can be tuned by adjusting the composition and morphology.[8] Furthermore, plasmonic and magnetic coupled nanoalloys can be created such as Au_xFe_{1-x} (ref. 9) and Co_xPt_{1-x} (ref. 10) for interesting magneto-optic coupling. Currently, most nanoalloys were grown through chemical synthesis methods which can produce effective nanoalloys. However, nanoalloys grown through these methods suffer from stability issues including dealloying and phase segregation.[3,11] Another major issue plaguing nanoalloys is the inability to easily tune their size, morphology, composition and properties.[1,4] To overcome the stability issues, multicomponent nanoalloys can be created but they also eventually suffer dealloying.[12] Another way is to create nanocomposites that encapsulate nanoalloys in a chemically stable nanocomposite form.[13]

Oxide-based nanocomposites present a promising platform for increasing long-term stability.[14] Oxides are typically chemically stable and have a wide range of functional properties like ferromagnetism in lanthanum strontium manganite (LSMO) or ferroelectricity in barium titanate (BTO). Combining different nanoalloys with different oxides could provide a pathway for achieving new, multifunctional hybrid materials with enhanced properties and stability. Growing these hybrid oxide–nanoalloy materials could be achieved through a pulsed laser deposition (PLD) technique. The PLD technique is a highly versatile physical vapor deposition method that has demonstrated a bottom-up, one-step method of growth for self-assembled oxide–metal hybrid materials such as $BaZrO_3$ (BZO)–Co, $BaTiO_3$ (BTO)–Au, ZnO–Au, and recently oxide–nanoalloy composites.[15–21] The PLD technique has already been used to achieve stability in oxide–metal and nitride–metal hybrid materials.[22–24] The critical issue to overcome for the oxide–nanoalloy system is to achieve a sufficiently mixed alloy without segregation.

In this work, the zinc oxide (ZnO) matrix has been combined with the Ag_xAu_{1-x} nanoalloy to form an oxide–nanoalloy hybrid plasmonic material of ZnO–Ag_xAu_{1-x}. The tunability of the oxide–nanoalloy ZnO–Ag_xAu_{1-x} hybrid material was investigated through manipulation of the oxygen background pressure during PLD. ZnO was selected as the matrix as it is a well-known wide-band gap semiconductor ($E_g \sim 3.37$ eV) that is useful for

[a]School of Materials Engineering, Purdue University, West Lafayette, Indiana 47907, USA. E-mail: hwang00@purdue.edu

[b]School of Electrical and Computer Engineering, Purdue University, West Lafayette, Indiana 47907, USA

[c]Sandia National Laboratory, Albuquerque, New Mexico, USA

† Electronic supplementary information (ESI) available. See DOI: 10.1039/d0na00887g

photocatalysis and transparent electrodes.[25–27] Furthermore, ZnO is chemically and thermally stable, earth abundant, and generally non-toxic, making it a promising candidate to form stable nanoalloy nanocomposites. Ag_xAu_{1-x} is chosen as the nanoalloy in this report due to it being extensively studied for its plasmonic resonance and usefulness in energy and sensor applications.[4,28] Varying the oxygen background pressure provides a successful method for tailoring the optical properties and morphology of ZnO–Ag_xAu_{1-x} nanocomposites. A highly tunable morphology can be achieved by systematic variation in background pressure as per the schematic presented in Fig. 1. As the background pressure varies from low pressure (vacuum and 20 mTorr) to high pressure (100 and 150 mTorr), the oxide–nanoalloy morphology could be effectively tuned. Systematic microstructural characterization of ZnO–Ag_xAu_{1-x} hybrid thin films was performed through XRD, STEM, and EDS-mapping and the corresponding effect on optical properties was investigated through spectroscopic ellipsometry and UV-vis spectroscopy.

Results and discussion

X-ray diffraction analysis was performed to elucidate the effect of oxygen background pressure on the morphology of ZnO–Ag_xAu_{1-x} nanocomposites. The results are summarized in Fig. 2. Scans of θ–2θ are depicted in Fig. 2a for all films deposited at different background pressures, indicating the high degree of epitaxial quality for all the films. The ZnO matrix grew in a hexagonal wurtzite structure with the preferred out-of-plane *c*-axis orientation along the (0002) direction, parallel with the underlying *c*-axis Al_2O_3 substrate (0006) plane. Both Ag and Au have a face-centered cubic (FCC) structure, and their alloys also form an FCC lattice.[29] Therefore, based on the measured θ–2θ, the alloy nanopillars were determined to have an FCC structure textured out-of-plane along the (111) direction and parallel to the (0006) plane of the substrate. To match both the hexagonal-shape of wurtzite ZnO and the *c*-axis oriented Al_2O_3 substrate, the alloy lattice rotates so that the out-of-plane direction has a 3-fold symmetry. This created an out-of-plane alignment of Ag_xAu_{1-x} $(lll)||$ZnO $(000l)||Al_2O_3$ $(000l)$.

To determine if there was peak splitting in the alloy, which could imply phase separation, high-resolution θ–2θ scans were performed across a small range near the (111) peak of Ag_xAu_{1-x}, as depicted in Fig. 2b. There is no obvious peak splitting, which implies that the nanoalloy grown in this work is well mixed for all samples. Interestingly, there are variations of peak position and *d*-spacing with respect to background pressure tuning. In Fig. 2b, the value of the location of bulk Ag ($2\theta_{111} = 38.116°$) and bulk Au ($2\theta_{111} = 38.252°$) peaks is denoted. For the nanoalloy deposited under vacuum, the peak was located near bulk Ag, with $2\theta_{111} = 38.11°$. As the background pressure was increased to 20 mTorr, the peak was shifted downward to below bulk Ag with $2\theta_{111} = 38.08°$. As the pressure was further increased to 100 mTorr and 150 mTorr, the peak shifted upward from $2\theta_{111} = 38.2°$ to $2\theta_{111} = 38.23°$. Interestingly, as the pressure was increased, the peak location shifted from near the Ag peak at low pressure toward the Au peak at high pressure. The relationship for tuning of the alloy lattice was more clearly demonstrated when investigating the *d*-spacing in Fig. 2d. For the films deposited under vacuum, the alloy *d*-spacing d_{111} is measured to be 0.2359 nm, which is the same as the bulk Ag *d*-spacing ($d_{111} = 0.2359$ nm). When background pressure increases to 150 mTorr, the alloy *d*-spacing d_{111} is measured to be 0.2352 nm, which is more comparable to bulk Au *d*-spacing ($d_{111} = 0.2351$ nm). When background pressure increases, compressive stress on the alloy lattice increases, as the *d*-spacing was tuned smaller from vacuum at $d_{111} = 0.2359$ nm to $d_{111} = 0.2352$ nm under the 150 mTorr conditions. The ZnO (0002) peak was also investigated to determine pressure variation, with high-resolution scans of the (0002) peak shown in Fig. 2c. There appeared to be some peak shifting with respect to background pressure, but no specific trend was observed. This was further confirmed based on the *d*-spacing of the ZnO (0002) peak in Fig. 2d, which shows no trend and little to no change in the ZnO lattice. This is contrary to the usual relationship between ZnO and the oxygen background pressure in PLD growth.[25,30–34] The lack of a general trend for the ZnO may be related to the nanoalloy formation driving the lattice strain in the nanocomposite.

The composition of each nanoalloy was calculated from the EDS-spectrum and plotted as a ratio of Ag/Au *vs.* background

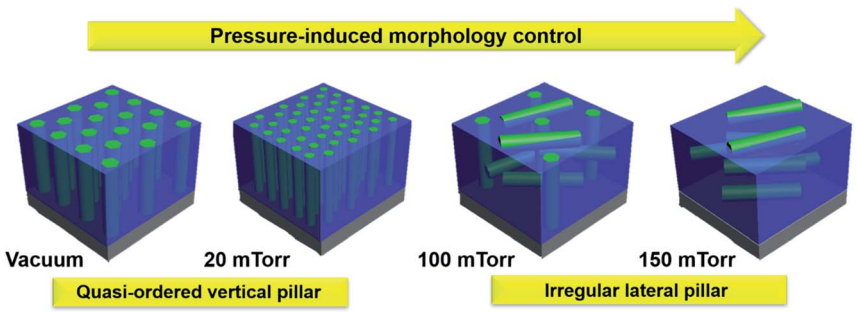

Fig. 1 Schematic diagram of oxygen pressure microstructure tuning in the ZnO– Ag_xAu_{1-x} nanocomposite. In the diagram, the ZnO matrix is colored blue while the Ag_xAu_{1-x} nanoalloy is colored green. Deposition at low pressure produces vertically aligned alloy nanopillars, while increasing oxygen pressure induces irregular lateral growth.

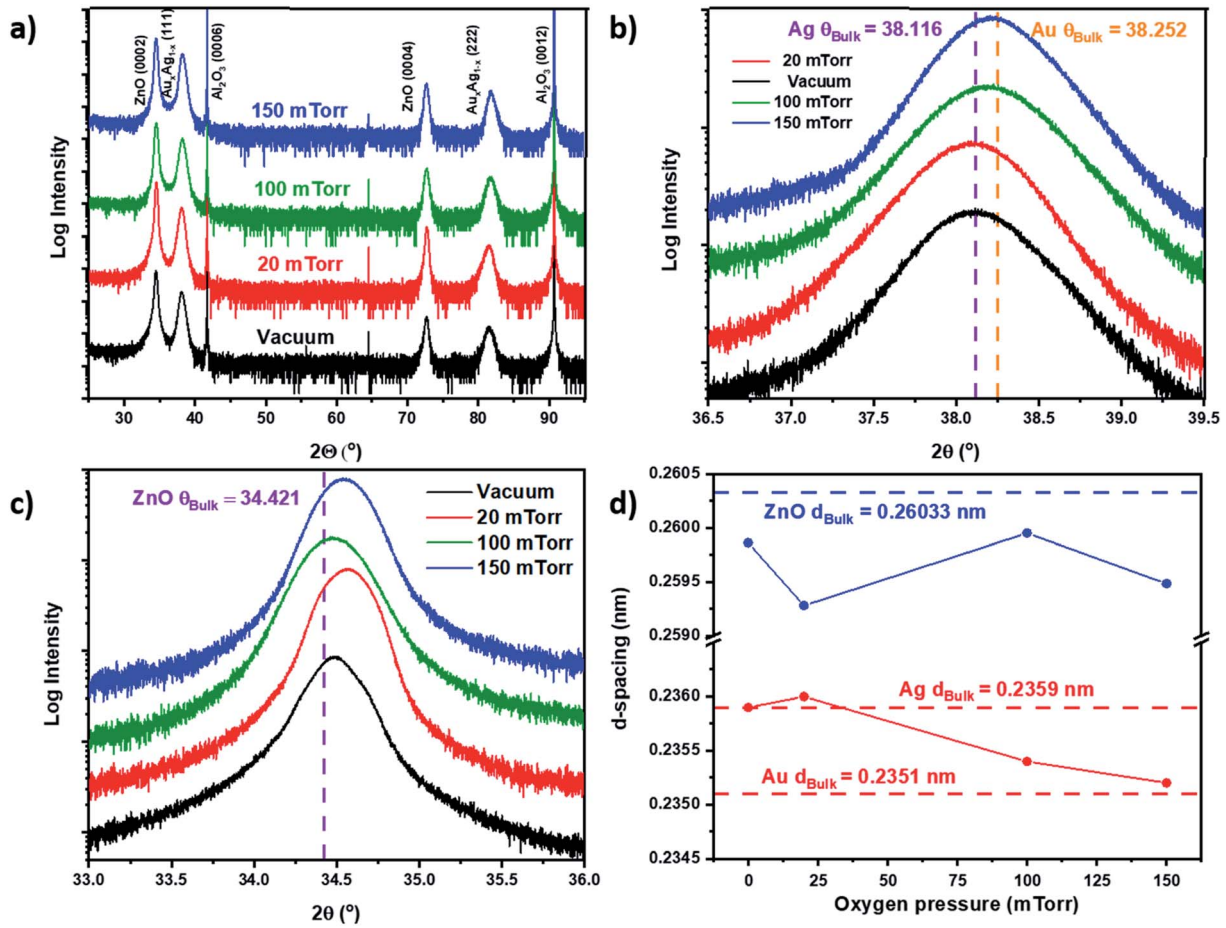

Fig. 2 X-ray diffraction. (a) Scans of θ–2θ for all films deposited at different oxygen pressures, (b) scans in the region of the Ag/Au (111) peak, (c) scans showing the region near the ZnO (0002) peak, and (d) d-spacing calculation for Ag_xAu_{1-x} (111) and ZnO (0002).

pressure in Fig. S1a – Ag†/Au > 1 implies Ag-rich alloys and Ag/Au < 1 implies Au-rich alloys. The resulting compositions from EDS-spectra are tabulated in Fig. S1b–e† and the Ag/Au *vs.* deposition pressure graph in Fig. S1a† was calculated using the wt% values from the tables in Fig. S1b–e.† The x-value for each nanoalloy composition was also calculated for each oxygen pressure deposition. Compositions of the nanoalloys were $Ag_{33}Au_{67}$, $Ag_{61}Au_{39}$, $Ag_{55}Au_{45}$, and $Ag_{67}Au_{33}$ for deposition under vacuum, 20 mTorr, 100 mTorr, and 150 mTorr, respectively. Results of the composition tuning and EDS show an overall trend of Ag content increasing with respect to increasing background pressure but there was a decrease in Ag content between 20 mTorr and 100 mTorr. The increase of Ag content and the decrease of Au could be related to the mass of Au and Ag and their kinetic energy during deposition. Ag is a lighter species than Au so it will have higher kinetic energy on initial ablation. Au will have lower kinetic energy than Ag and therefore as the pressure is increased, Au species will show less diffusion in the film.

For more detailed microstructural characterization, the ZnO–$Ag_{33}Au_{67}$ vertically-aligned nanocomposite (VAN) deposited in vacuum was selected for a microscopy analysis. The full characterization results using STEM coupled with EDS-mapping and TEM are depicted in Fig. 3. A model of the structure can be seen in Fig. 3a of the VAN. A STEM image of the cross-sectional sample is shown in Fig. 3b. HR-STEM was performed in Fig. 3c to determine the atomic arrangement of $Ag_{33}Au_{67}$ and ZnO. The blue-dashed line indicates the heterointerface between the ZnO matrix and nanopillars. The out-of-plane atomic arrangement of $Ag_{33}Au_{67}$ grows in the out-of-plane direction [111] and ZnO grows in the out-of-plane direction [0002], confirming the orientation from XRD in Fig. 2. STEM coupled with EDS-mapping was performed on the cross-sectional image in Fig. 3d–g. The map of Au can be seen in Fig. 3d and Ag is in Fig. 3e. Mapping of Ag and Au only occurred from the nanopillar and mapping of Zn only occurred in the matrix, indicating the well separated nanopillar and matrix phases. A STEM image of the plan-view is shown in Fig. 3h, depicting a hexagonal shape of alloy nanopillars and quasi-hexagonal in-plane ordering. Plan-view EDS-mapping was performed in Fig. 3j–m to confirm the well-separated phases of Ag_xAu_{1-x} pillars and the ZnO matrix, as evidenced by the Ag, Au and Zn maps and the combined EDS-map in Fig. 3l. A HR-TEM plan-view image in Fig. 3m shows the in-plane atomic arrangement of nanopillars and the matrix. The (111) stacking arrangement of the alloy pillars can be seen as the wurtzite structure of the matrix, and

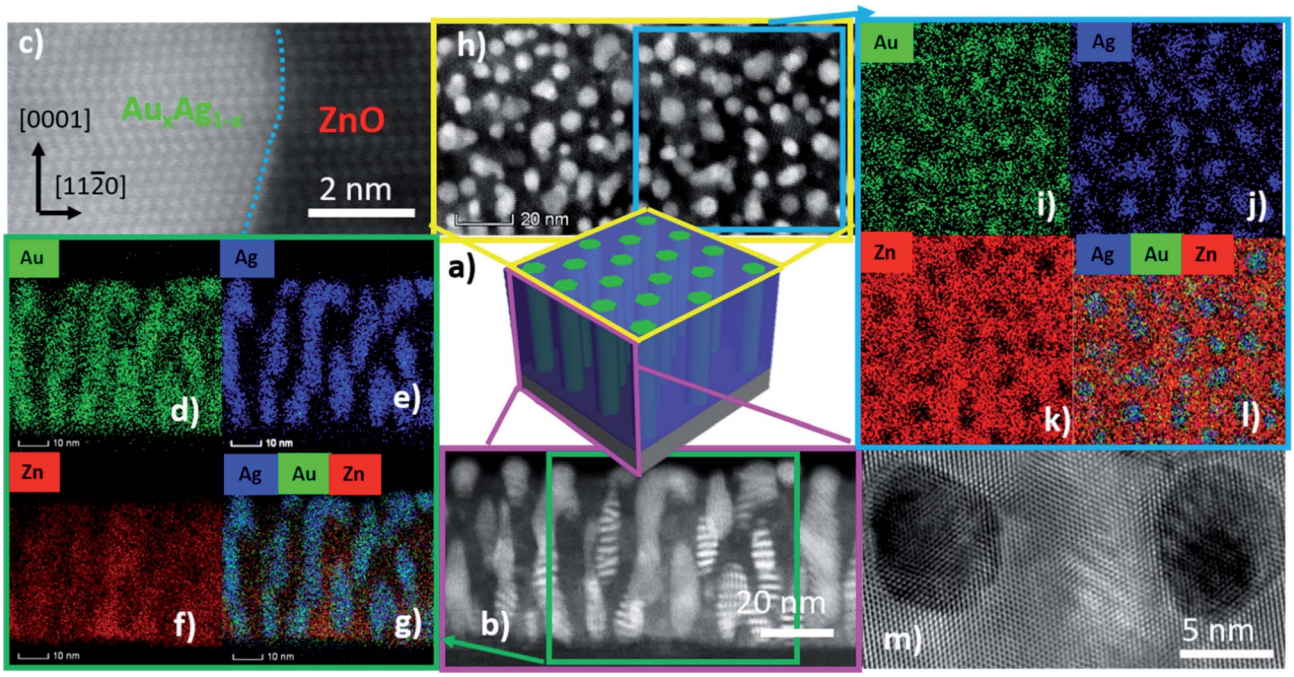

Fig. 3 Microstructure characterization of the vacuum deposited sample. (a) schematic diagram of the microstructure, (b) representative cross-sectional STEM micrograph, (c) HRSTEM micrograph at the heterointerface of the alloy/oxide. EDS-chemical map of (d) Au, (e) Ag, (f) Zn, and (g) combined. (h) Representative plan-view micrograph. EDS-mapping of (i) Au, (j) Zn, and (k) combined. (m) HRTEM of plan-view specimen.

the sides of the nanoalloy nanopillars are indexed as {220} planes. The out-of plane epitaxial relationship is determined from the cross-sectional SAED pattern in Fig. S2† as $Ag_{33}Au_{67}$ (220)||ZnO (10-10)||Al_2O_3 (11-20); the in-plane epitaxial relationship was determined as $Ag_{33}Au_{67}$ (20-2)||ZnO (11-20)||Al_2O_3 (01-10). Moreover, the in-plane diffraction pattern of the alloy demonstrated interesting double-diffraction in the SAED pattern relating to the alloy formation.

The effect of oxygen background pressure on the morphology of ZnO–Ag_xAu_{1-x} nanocomposites was investigated through scanning transmission electron microscopy (STEM) analysis of both cross-sectional and plan-view samples of all the films for comparison in Fig. 4. STEM under high angle annular dark field mode (HAADF) was chosen as it provides excellent composition related contrast due to *Z*-contrast imaging (*i.e.*, contrast $\sim Z^{1.7}$). Furthermore, cross-sectional EDS-mapping was also performed on the other nanoalloy samples deposited at different background pressures and is presented in Fig. S3.† The EDS-map of each film shows that the nanoalloy remained sufficiently mixed despite systematic increases in background deposition pressure. Moreover, the nanoalloy and the oxide matrix remained as a distinctly two-phase nanocomposite material. The cross-sectional STEM image of the film deposited under vacuum is shown in Fig. 4a. The morphology comprised vertically aligned alloy nanopillars embedded in the ZnO matrix. The plan-view STEM image under vacuum is shown in Fig. 4e, and indicates that alloy nanopillars have a hexagonal shape, which followed from the XRD pattern of the alloy having the out-of-plane (111) direction. Interestingly, as background pressure was increased to 20 mTorr in Fig. 4b, the pillars remained vertically aligned but are at higher density and some particles become interspersed in the matrix. The plan-view of

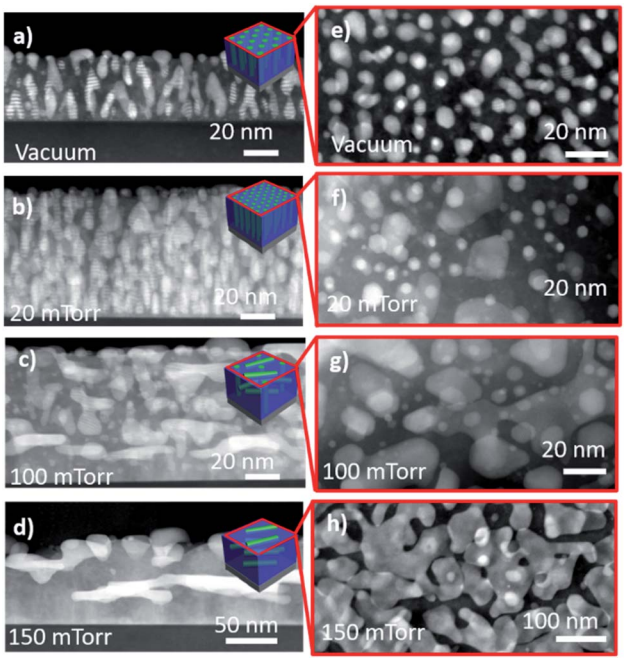

Fig. 4 Morphology tuning through oxygen pressure. Cross-sectional STEM image for (a) vacuum, (b) 20 mTorr, (c) 100 mTorr, and (d) 150 mTorr. Corresponding plan-view image for (e) vacuum, (f) 20 mTorr, (g) 100 mTorr, and (h) 150 mTorr.

the 20 mTorr film in Fig. 4f indicated that nanopillars retained the hexagonal shape and confirmed the increase in small particles when compared to the film grown under vacuum in Fig. 4e. When background pressure was increased to 100 mTorr in Fig. 4c, the morphology became more irregular and included a combination of vertical and lateral growth. This suggests that morphology tuning could be caused by the increased background pressure and reduced kinetic energy, and resulting in plasma plume cluster nucleation as reported previously.[35] In the plan-view image shown in Fig. 4g, the 100 mTorr growth retained some hexagonal morphology of nanopillars and increased in size. The background pressure was further increased to 150 mTorr in Fig. 4d, where the morphology became more regular and lateral. This is confirmed in Fig. 4h, where the growth is depicted as irregularly shaped lateral nanopillars. As background pressure was increased, the ordering of the nanopillars appears to become more irregular within the matrix. Under higher pressure, there is a reduction in kinetic energy and consequently, resulting in irregular nanopillar growth. Moreover, as the background pressure is increased, cluster nucleation begins to occur in the plasma plume.[36–39] This cluster nucleation and reduction in kinetic energy could be accounted for the transition from vertical pillars at low pressure to lateral pillars under high pressure. The reduction in kinetic energy inhibits the ability for ordered and vertically aligned pillar formation. Moreover, the reduction in kinetic energy in the plasma plume causes the ejection of heavier elements like Au, which could explain the observed composition tuning in Fig. S1† such that the Ag content increases in the nanoalloy as pressure is increased.

Bimetallic Ag_xAu_{1-x} nanoalloys are beneficial for their plasmonic response. The optical properties of ZnO–Ag_xAu_{1-x} oxide–alloy nanocomposites deposited at different background pressures were investigated through UV-vis spectroscopy, as depicted in Fig. 5. The surface plasmon resonance of each film is indicated by a minimum in each plot and marked in the figure. For the nanocomposite deposited under vacuum, there is a surface plasmon resonance at 492 nm. As the background pressure increases to 20 mTorr, the plasmonic resonance is 512 nm. At 150 mTorr, the surface plasmon is further red shifted to 545 nm and the plasmonic resonance at 150 mTorr is 595 nm. Here, a red shift of the plasmonic resonance with increasing background pressure is observed. The tuning of the plasmon resonance from 492 nm under vacuum to 595 nm at 150 mTorr could be related to the effective microstructure and morphology tuning as discussed above. Specifically, increasing the background pressure will cause a red shift of the plasmon resonance. Interestingly, the red-shift with increasing Ag content is converse to what is usually observed. Therefore, the morphology tuning might be one of the dominant factors in terms of plasmon resonance tuning as growing more lateral pillars from vacuum to 150 mTorr resulted in red-shifted plasmon resonance. The significant morphology variation from vertically aligned pillars at low pressure to the lateral pillar at high pressure could result in a transition of different plasmon excitation.[40] In the UV-vis measurement, the light beam is traveling through the film, such that at low pressure the transverse plasmon resonance is more dominantly excited. As the pressure increases and the morphology of the pillars becomes lateral, it could be that the longitudinal plasmon resonance is more dominantly excited. On the other hand, composition tuning could also play a role in the tuning effect, as the Au content is found to drop with increasing background pressure, as evidenced in Fig. S1.† More detailed studies are needed to clearly understand the mechanism of plasmon tuning in this system.

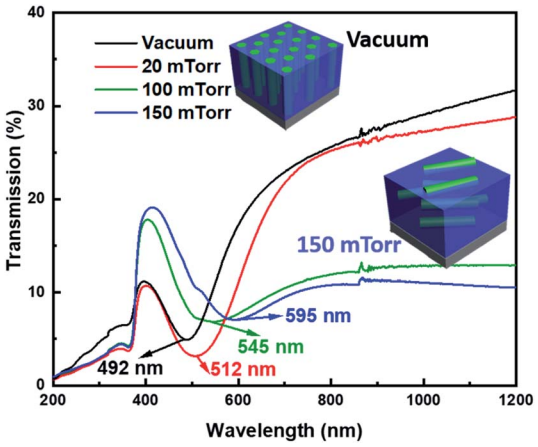

Fig. 5 Transmission UV-vis spectrum showing optical tuning, numbers on graph indicate the plasmonic peak.

Because of the anisotropic nature of the hybrid nanoalloy morphology, the dielectric function and anisotropic optical properties were analysed by spectroscopic ellipsometry (see methods) . The experimental setup and the imaginary permittivity for each film can be found in Fig. S4.† Data for the measured ellipsometry parameters of psi and delta and corresponding models can be found in Fig. S5 and S6.† The real part of the permittivity for each hybrid thin film deposited at different background pressures is plotted in Fig. 6. All films demonstrate the properties of hyperbolic metamaterials (HMM) and the hyperbolic dispersion is coupled with epsilon near zero permittivity (ENZ). HMMs have a dielectric function that acts as a metal in one direction and a dielectric in the perpendicular direction.[41] In Fig. 6, the region for hyperbolic dispersion is marked on each graph. A type I HMM with an isofrequency curve of a hyperboloid of two sheets that can support only high k states is denoted in the graphs in Fig. 6 as a purple region. The type II HMM with an isofrequency curve of a paraboloid of one sheet that can support both high and low k states is denoted with a yellow shading. Representative isofrequency curves are shown in the inset of the graphs of Fig. 6.

Angular dependent ellipsometry data were measured and fitted for all the samples. The real part of permittivity for the vacuum deposited film can be found in Fig. 6a. This film is a type II HMM with a hyperbolic region spanning parts of the visible and near-infrared (NIR) from 593 nm to 1023 nm. In this region, the components out-of-plane to the anisotropy axis $\varepsilon_\perp < 0$ and in-plane to the anisotropy axes $\varepsilon_\parallel > 0$ and $\varepsilon_\perp$ have ENZ permittivity at 593 nm and 1023 nm. The real part of

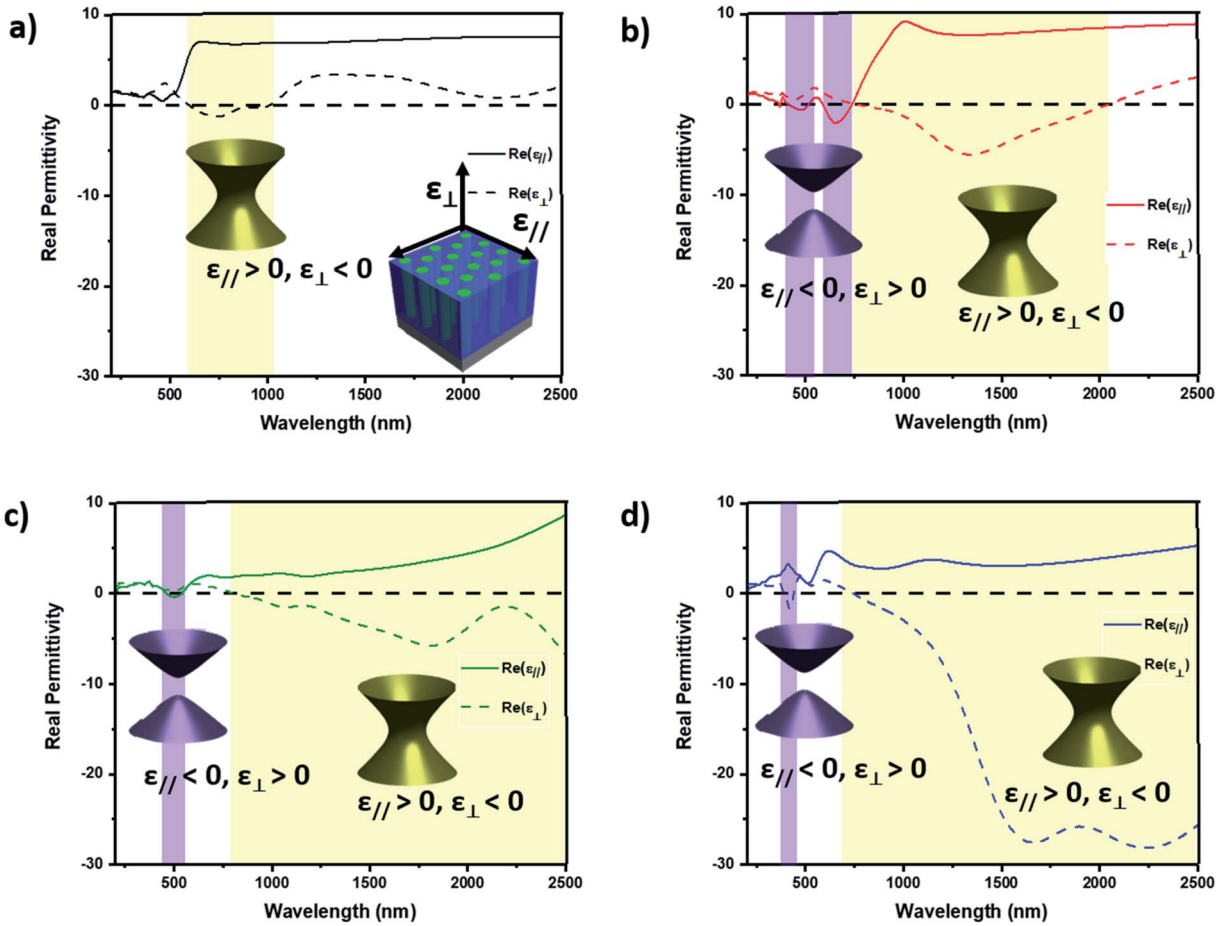

Fig. 6 Dielectric function tuning. Real part of dielectric function for (a) vacuum, (b) 20 mTorr, (c) 100 mTorr and (d) 150 mTorr. Inset shows representative isofrequency curves indicating the type of hyperbolic metamaterial, yellow represents a type I hyperbolic metamaterial with the surface of a hyperboloid of one sheet and purple represents a type II hyperbolic metamaterial with the surface of a hyperboloid of two sheets.

permittivity of the film deposited at 20 mTorr is depicted in Fig. 6b. Upon increasing the background pressure to 20 mTorr, the type II hyperbolic region in the visible-near infrared region increases in size to include a range of 736–2050 nm. Moreover, two new type I hyperbolic regions occur from 400 to 520 nm and 590 to 736 nm, where $\varepsilon_{\parallel} < 0$ and $\varepsilon_{\perp} > 0$. The out-of-plane ($\varepsilon_{\perp}$) component has ENZ permittivity at 736 and 2060 nm and the in-plane ($\varepsilon_{\parallel}$) component has ENZ permittivity at 400, 520, 590, and 736 nm. Upon increasing background deposition pressure to 100 mTorr, the hyperbolic properties are further tuned. In the 100 mTorr deposited film, the type II region now spans from 788 to 2500 nm, the end of the measured spectrum. Compared with the 20 mTorr film, there is only one type I region occurring from 463–560 nm. The in-plane component has ENZ permittivity at 463 and 560 nm while the out-of-plane component has ENZ permittivity at around 788 nm. Further increasing the background deposition pressure to 150 mTorr maintained the type II region and decreased the size of the region in the visible region and it is changed to type II hyperbolic dispersion. The real part of the permittivity for the 150 mTorr sample is plotted in Fig. 6d. The type II HMM region occurs from 740 to 2500 nm and 387 to 440 nm. The in-plane component has ENZ permittivity at 387, 440 nm, and 740 nm. Pressure induced dielectric function tuning has also been observed in the ZnO–Au VAN system.[20]

The work in this report demonstrates the robust tunability of the hybrid plasmonic ZnO–Ag_xAu_{1-x} system and the respective effect on morphology and material properties. Thin films grown under vacuum produce vertically aligned nanoalloy pillars that can be tuned more laterally by introducing and increasing the oxygen background pressure during growth. The change in the morphology also leads to tunability of the optical properties and composition of the nanoalloy, where increasing oxygen pressure will decrease Au and red-shift the plasmonic response. Due to the self-assembled nature of the growth and one-step PLD approach, there are a robust number of parameters that can be tuned to achieve new oxide–nanoalloy morphology and property effects. Future studies could investigate the result of frequency, substrate temperature, or laser energy tuning on the ZnO–Ag_xAu_{1-x}. Moreover, due to the ZnO support and highly tailorable morphology, the ZnO–Ag_xAu_{1-x} system broadens the applicability of nanoalloy thin films toward future integrations where previous nanoalloys are restricted in their use due to instability. Due to the robustness of the oxide–nanoalloy approach, other

nanoalloys can be explored such as magneto-optic candidates like Ni_xCu_{1-x} or Ni_xAu_{1-x} and other plasmonic candidates like Ag_xCu_{1-x} and Ag_xAl_{1-x}. This hybrid ZnO–Ag_xAu_{1-x} system with tunable optical properties, such as a tailorable plasmon resonance range, could find applications as optical device components that require a specific wavelength range in optical absorption, sensing and detection.

Conclusion

In this work, ZnO–Ag_xAu_{1-x} nanocomposite thin films with highly tunable morphology, composition, and optical properties were demonstrated. The films were deposited at different background pressures, each with unique morphology and properties. The film deposited in vacuum has a vertically aligned nanopillar structure, which was tuned toward irregular lateral nanopillar growth at high background pressure. The hybrid oxide–nanoalloy materials in this report demonstrated strong plasmonic resonance in the UV-vis region that was highly tunable. Moreover, due to the inherent anisotropy of the nanocomposite morphology, they have interesting anisotropic dielectric function with hyperbolicity at useful wavelengths. We found the film deposited at 20 mTorr, with high density pillar morphology, to have the most interesting optical properties in terms of practical applications due to a broad wavelength range of hyperbolic dielectric functions and relatively low absorption. This work presents broad tunability in hyperbolicity and plasmonic properties using the design of metallic alloy nanopillars in an oxide matrix to address the versatile optical property needs in optical components and devices.

Experimental

Thin film growth

ZnO–Ag_xAu_{1-x} nanocomposite films were grown on c-cut Al_2O_3 (0001) using pulsed laser deposition. Growth was performed with a KrF excimer laser (Lambda Physik Complex Pro 205, $\lambda =$ 248 nm) and the substrate temperature was kept constant at 500 °C. The laser energy was 420 mJ and focused at an incident angle of 45°. The target–substrate distance was kept constant at 4.5 cm and measured before each deposition to ensure accuracy. A composite target consisting of ZnO–Ag_xAu_{1-x} was developed through solid-state sintering used for laser ablation. Before deposition, the chamber was pumped down to around 10^{-6} mTorr before oxygen pressure was applied. Oxygen background pressure was varied from vacuum to 150 mTorr and the laser pulse frequency was set to 5 Hz for all depositions. After all depositions, the chamber was cooled to room temperature at a rate of 15 °C min^{-1}.

Microstructure characterization

The film morphology was characterized through XRD, TEM, and STEM coupled with EDS-mapping. XRD scans of θ–2θ were conducted using a Panalytical X'Pert X-ray diffractometer with Cu K_α radiation. Bright field TEM, STEM, SAED and EDS-mapping were performed on a FEI Talos F200X TEM. Samples for electron microscopy were prepared, for both cross-sectional and plan-view, *via* a standard grinding procedure which entails manual grinding, polishing, dimpling, and a final ion milling step to achieve electron transparency (PIPS 691 precision ion polishing system, 5 keV for cross-section and 4–4.5 keV for plan-view samples).

Optical measurements

Ellipsometry experiments were carried out on an RC2 Spectroscopic ellipsometer (J.A. Woollam Company). Three angles 30°, 45°, and 60° were measured from a spectrum range of 210–2500 nm. Measured values of psi and delta data were obtained and then fit with a uniaxial model coupled with a B-spline model to discern the anisotropic dielectric function of ZnO–Ag_xAu_{1-x} nanocomposite thin films, and an agreeable mean square error (MSE) < 5 was obtained for all film models. Normal incident depolarized transmittance (T%) was measured using an optical spectrophotometer (Lambda 1050 UV-vis spectrophotometer).

Conflicts of interest

There are no conflicts to report.

Acknowledgements

This work was supported by the U.S. Department of Energy, Office of Science, Basic Energy Sciences under Award DE-SC0020077. R. L. P. acknowledges the support from the Laboratory Directed Research and Development program at Sandia National Laboratories, a multimission laboratory managed and operated by National Technology and Engineering Solutions of Sandia, LLC., a wholly owned subsidiary of Honeywell International, Inc., for the U.S. Department of Energy's National Nuclear Security Administration under contract DE-NA-003525. R. L. P. also acknowledges the funding support from the Purdue Doctoral Fellow program. X. S. acknowledges the support from the U.S. National Science Foundation (DMR-1565822) for the TEM characterization effort. The paper describes objective technical results and analysis. Any subjective views or opinions that might be expressed in the paper do not necessarily represent the views of the U.S. Department of Energy or the United States Government.

References

1 H. Fang, J. Yang, M. Wen and Q. Wu, Nanoalloy Materials for Chemical Catalysis, *Adv. Mater.*, 2018, **30**(17), 1–10, DOI: 10.1002/adma.201705698.
2 R. Ferrando, R. L. Johnston and C. Louis, Recent Advances in the Chemical Physics of Nanoalloys, *Phys. Chem. Chem. Phys.*, 2015, **17**(42), 27920–27921, DOI: 10.1039/c5cp90142a.
3 R. Ferrando, J. Jellinek and R. L. Johnston, Nanoalloys: From Theory to Applications of Alloy Clusters and Nanoparticles, *Chem. Rev.*, 2008, **108**(3), 845–910, DOI: 10.1021/cr040090g.

4 B. M. Muñoz-Flores, B. I. Kharisov, V. M. Jiménez-Pérez, P. Elizondo Martínez and S. T. López, Recent Advances in the Synthesis and Main Applications of Metallic Nanoalloys, *Ind. Eng. Chem. Res.*, 2011, **50**(13), 7705–7721, DOI: 10.1021/ie200177d.

5 I. Chanu, P. Krishnamurthi and P. T. Manoharan, Effect of Silver on Plasmonic, Photocatalytic, and Cytotoxicity of Gold in AuAgZnO Nanocomposites, *J. Phys. Chem. C*, 2017, **121**(16), 9077–9088, DOI: 10.1021/acs.jpcc.7b02232.

6 H. Prunier, J. Nelayah, C. Ricolleau, G. Wang, S. Nowak, A. F. Lamic-Humblot and D. Alloyeau, New Insights into the Mixing of Gold and Copper in a Nanoparticle from a Structural Study of Au–Cu Nanoalloys Synthesized *via* a Wet Chemistry Method and Pulsed Laser Deposition, *Phys. Chem. Chem. Phys.*, 2015, **17**(42), 28339–28346, DOI: 10.1039/c5cp01491c.

7 Ö. Çelik and T. Fırat, Synthesis of FeCo Magnetic Nanoalloys and Investigation of Heating Properties for Magnetic Fluid Hyperthermia, *J. Magn. Magn. Mater.*, 2018, **456**, 11–16, DOI: 10.1016/j.jmmm.2018.01.090.

8 I. Robinson, S. Zacchini, L. D. Tung, S. Maenosono and N. T. K. Thanh, Fisica Synthesis and Characterization of Magnetic Nanoalloys from Bimetallic Carbonyl Clusters, *Chem. Mater.*, 2009, **21**(13), 3021–3026, DOI: 10.1021/cm9008442.

9 V. Amendola, S. Scaramuzza, S. Agnoli, S. Polizzi and M. Meneghetti, Strong Dependence of Surface Plasmon Resonance and Surface Enhanced Raman Scattering on the Composition of Au–Fe Nanoalloys, *Nanoscale*, 2014, **6**(3), 1423–1433, DOI: 10.1039/c3nr04995g.

10 I. Parsina, C. Dipaola and F. Baletto, A Novel Structural Motif for Free CoPt Nanoalloys, *Nanoscale*, 2012, **4**(4), 1160–1166, DOI: 10.1039/c1nr11171j.

11 G. Barcaro, L. Sementa and A. Fortunelli, Simulation of Supported Metal Clusters, in *Encyclopedia of Nanotechnology*, ed. B. Bhushan, Springer, Dordrecht, 2015, DOI: 10.1007/978-94-007-6178-0_100948-1.

12 J. Zhao, K. Jarvis, P. Ferreira and A. Manthiram, Performance and Stability of Pd–Pt–Ni Nanoalloy Electrocatalysts in Proton Exchange Membrane Fuel Cells, *J. Power Sources*, 2011, **196**(10), 4515–4523, DOI: 10.1016/j.jpowsour.2011.01.026.

13 N. Alissawi, V. Zaporojtchenko, T. Strunskus, I. Kocabas, V. S. K. Chakravadhanula, L. Kienle, D. Garbe-Schönberg and F. Faupel, Effect of Gold Alloying on Stability of Silver Nanoparticles and Control of Silver Ion Release from Vapor-Deposited Ag–Au/Polytetrafluoroethylene Nanocomposites, *Gold Bull.*, 2013, **46**(1), 3–11, DOI: 10.1007/s13404-012-0073-6.

14 tefan Neatu, J. A. Maciá-Agullò, P. Concepciòn and H. Garcia, Gold–Copper Nanoalloys Supported on TiO_2 as Photocatalysts for CO_2 Reduction by Water, *J. Am. Chem. Soc.*, 2014, **136**(45), 15969–15976, DOI: 10.1021/ja506433k.

15 J. Huang, L. Li, P. Lu, Z. Qi, X. Sun, X. Zhang and H. Wang, Self-Assembled Co–$BaZrO_3$ Nanocomposite Thin Films with Ultra-Fine Vertically Aligned Co Nanopillars, *Nanoscale*, 2017, **9**(23), 7970–7976, DOI: 10.1039/c7nr01122a.

16 B. Zhang, M. Fan, L. Li, J. Jian, J. Huang, H. Wang, M. Kalaswad and H. Wang, Tunable Magnetic Anisotropy of Self-Assembled Fe Nanostructures within a $La_{0.5}Sr_{0.5}FeO_3$ Matrix, *Appl. Phys. Lett.*, 2018, **112**(1), 5, DOI: 10.1063/1.5008382.

17 L. Li, L. Sun, J. S. Gomez-Diaz, N. L. Hogan, P. Lu, F. Khatkhatay, W. Zhang, J. Jian, J. Huang, Q. Su, M. Fan, C. Jacob, J. Li, X. Zhang, Q. Jia, M. Sheldon, A. Alù, X. Li and H. Wang, Self-Assembled Epitaxial Au-Oxide Vertically Aligned Nanocomposites for Nanoscale Metamaterials, *Nano Lett.*, 2016, **16**(6), 3936–3943, DOI: 10.1021/acs.nanolett.6b01575.

18 S. Misra, L. Li, D. Zhang, J. Jian, Z. Qi, M. Fan, H. T. Chen, X. Zhang and H. Wang, Self-Assembled Ordered Three-Phase Au–$BaTiO_3$–ZnO Vertically Aligned Nanocomposites Achieved by a Templating Method, *Adv. Mater.*, 2019, **31**(7), 1–8, DOI: 10.1002/adma.201806529.

19 S. Misra, L. Li, J. Jian, J. Huang, X. Wang, D. Zemlyanov, J. Jang, F. H. Ribeiro and H. Wang, Tailorable Au Nanoparticles Embedded in Epitaxial TiO_2 Thin Films for Tunable Optical Properties, *ACS Appl. Mater. Interfaces*, 2018, **10**, 32895–32902, DOI: 10.1021/acsami.8b12210.

20 R. L. Paldi, X. Sun, X. Wang, X. Zhang and H. Wang, Strain-Driven In-Plane Ordering in Vertically Aligned ZnO–Au Nanocomposites with Highly Correlated Metamaterial Properties, *ACS Omega*, 2020, **5**(5), 2234–2241, DOI: 10.1021/acsomega.9b03356.

21 R. L. Paldi, X. Wang, X. Sun, Z. He, Z. Qi, X. Zhang and H. Wang, Vertically Aligned Ag_xAu_{1-x} Alloyed Nanopillars Embedded in ZnO as Nanoengineered Low-Loss Hybrid Plasmonic Metamaterials, *Nano Lett.*, 2020, **20**(5), 3778–3785, DOI: 10.1021/acs.nanolett.0c00790.

22 X. Wang, J. Jian, S. Diaz-Amaya, C. E. Kumah, P. Lu, J. Huang, D. G. Lim, V. G. Pol, J. P. Youngblood, A. Boltasseva, L. A. Stanciu, D. M. O'Carroll, X. Zhang and H. Wang, Hybrid Plasmonic Au–TiN Vertically Aligned Nanocomposites: A Nanoscale Platform towards Tunable Optical Sensing, *Nanoscale Adv.*, 2019, **1**(3), 1045–1054, DOI: 10.1039/c8na00306h.

23 J. Huang, X. Wang, N. L. Hogan, S. Wu, P. Lu, Z. Fan, Y. Dai, B. Zeng, R. Starko-Bowes, J. Jian, H. Wang, L. Li, R. P. Prasankumar, D. Yarotski, M. Sheldon, H. T. Chen, Z. Jacob, X. Zhang and H. Wang, Nanoscale Artificial Plasmonic Lattice in Self-Assembled Vertically Aligned Nitride–Metal Hybrid Metamaterials, *Adv. Sci.*, 2018, **5**(7), 1800416, DOI: 10.1002/advs.201800416.

24 J. Huang, X. Wang, X. L. Phuah, P. Lu, Z. Qi and H. Wang, Plasmonic Cu Nanostructures in ZnO as Hyperbolic Metamaterial Thin Films, *Mater. Today Nano*, 2019, **8**, 100052, DOI: 10.1016/j.mtnano.2019.100052.

25 R. Kumar, G. Kumar and A. Umar, Pulse Laser Deposited Nanostructured Zno Thin Films: A Review, *J. Nanosci. Nanotechnol.*, 2014, **14**(2), 1911–1930, DOI: 10.1166/jnn.2014.9120.

26 S. M. Chou, L. G. Teoh, W. H. Lai, Y. H. Su and M. H. Hon, ZnO:Al Thin Film Gas Sensor for Detection of Ethanol Vapor, *Sensors*, 2006, **6**(10), 1420–1427, DOI: 10.3390/s6101420.

27 B. Parida, S. Iniyan and R. Goic, A Review of Solar Photovoltaic Technologies, *Renewable Sustainable Energy Rev.*, 2011, **15**(3), 1625–1636, DOI: 10.1016/j.rser.2010.11.032.

28 T. Chung, C. S. H. Hwang, M. S. Ahn and K. H. Jeong, Au/Ag Bimetallic Nanocomposites as a Highly Sensitive Plasmonic Material, *Plasmonics*, 2019, **14**(2), 407–413, DOI: 10.1007/s11468-018-0818-z.

29 L. W. McKeehan, The Crystal Structure of Silver–Palladium and Silver–Gold Alloys, *Phys. Rev.*, 1922, **20**(5), 424–432, DOI: 10.1103/PhysRev.20.424.

30 S. Choopun, R. D. Vispute, W. Noch, A. Balsamo, R. P. Sharma, T. Venkatesan, A. Iliadis and D. C. Look, Oxygen Pressure-Tuned Epitaxy and Optoelectronic Properties of Laser-Deposited ZnO Films on Sapphire, *Appl. Phys. Lett.*, 1999, **75**(25), 3947–3949, DOI: 10.1063/1.125503.

31 T. Bando, K. Abe and M. Yamashita, Effect of ZnO Plasma Plume Dynamics on Laser Ablation, *Opt. Rev.*, 2010, **17**(3), 309–312.

32 Z. G. Zhang, F. Zhou, X. Q. Wei, M. Liu, G. Sun, C. S. Chen, C. S. Xue, H. Z. Zhuang and B. Y. Man, Effects of Oxygen Pressures on Pulsed Laser Deposition of ZnO Films, *Phys. E*, 2007, **39**(2), 253–257, DOI: 10.1016/j.physe.2007.05.028.

33 J. H. Lee, C.-Y. Chou, Z. Bi, C.-F. Tsai and H. Wang, Growth-Controlled Surface Roughness in Al-Doped ZnO as Transparent Conducting Oxide, *Nanotechnology*, 2009, **20**(39), 395704, DOI: 10.1088/0957-4484/20/39/395704.

34 J. B. Franklin, B. Zou, P. Petrov, D. W. McComb, M. P. Ryan and M. A. McLachlan, Optimised Pulsed Laser Deposition of ZnO Thin Films on Transparent Conducting Substrates, *J. Mater. Chem.*, 2011, **21**(22), 8178–8182, DOI: 10.1039/c1jm10658a.

35 M. S. Tillack, D. W. Blair and S. S. Harilal, The Effect of Ionization on Cluster Formation in Laser Ablation Plumes, *Nanotechnology*, 2004, **15**(3), 390–403, DOI: 10.1088/0957-4484/15/3/028.

36 A. Sambri, A. Khare, S. Mirabella, E. Di Gennaro, A. Safeen, F. Di Capua, L. Campajola, U. Scotti Di Uccio, S. Amoruso and F. Miletto Granozio, Plasma Dynamics and Cations Off-Stoichiometry in $LaAlO_3$ films Grown in High Pressures Regimes, *J. Appl. Phys.*, 2016, **120**(22), 225306, DOI: 10.1063/1.4971766.

37 A. V. Bulgakov and N. M. Bulgakova, Gas-Dynamic Effects of the Interaction between a Pulsed Laser-Ablation Plume and the Ambient Gas: Analogy with an Underexpanded Jet, *J. Phys. D: Appl. Phys.*, 1998, **31**(6), 693–703, DOI: 10.1088/0022-3727/31/6/017.

38 A. V. Bulgakov and N. M. Bulgakova, Dynamics of Laser-Induced Plume Expansion into an Ambient Gas during Film Deposition, *J. Phys. D: Appl. Phys.*, 1995, **28**(8), 1710–1718, DOI: 10.1088/0022-3727/28/8/022.

39 S. Wicklein, A. Sambri, S. Amoruso, X. Wang, R. Bruzzese, A. Koehl and R. Dittmann, Pulsed Laser Ablation of Complex Oxides: The Role of Congruent Ablation and Preferential Scattering for the Film Stoichiometry, *Appl. Phys. Lett.*, 2012, **101**(13), 131601, DOI: 10.1063/1.4754112.

40 J. Cao, T. Sun and K. T. V. Grattan, Gold Nanorod-Based Localized Surface Plasmon Resonance Biosensors: A Review, *Sens. Actuators, B*, 2014, **195**, 332–351, DOI: 10.1016/j.snb.2014.01.056.

41 A. Poddubny, I. Iorsh, P. Belov and Y. Kivshar, Hyperbolic Metamaterials, *Nat. Photonics*, 2013, **7**(12), 958–967, DOI: 10.1038/nphoton.2013.243.